HHS Public Access

Author manuscript

Magn Reson Med. Author manuscript; available in PMC 2017 April 01.

Published in final edited form as:

Magn Reson Med. 2016 April ; 75(4): 1434–1443. doi:10.1002/mrm.25675.

Single-Breath Clinical Imaging of Hyperpolarized ^{129}Xe in the Airspaces, Barrier, and Red Blood Cells using an Interleaved 3D Radial 1-Point Dixon Acquisition

S. Sivaram Kaushik[1,2], **Scott H. Robertson**[1,3], **Matthew S. Freeman**[1,3], **Mu He**[1,4], **Kevin T. Kelly**[5], **Justus E. Roos**[6], **Craig R. Rackley**[6], **W. Michael Foster**[7], **H. Page McAdams**[6], and **Bastiaan Driehuys**[1,2,3,6]

[1]Center for In Vivo Microscopy, Duke University, Durham NC

[2]Dept. of Biomedical Engineering, Duke University, Durham NC

[3]Graduate Program in Medical Physics, Duke University, Durham NC

[4]Dept. of Electrical Engineering, Duke University, Durham NC

[5]Radiation Oncology, Duke University, Durham NC

[6]Radiology, Duke University, Durham NC

[7]Dept. of Pulmonary and Critical Care Medicine, Duke University, Durham NC

Abstract

Purpose—We sought to develop and test a clinically feasible 1-point Dixon, 3D radial acquisition strategy to create isotropic 3D MR images of ^{129}Xe in the airspaces, barrier, and red blood cells (RBCs) in a single breath. The approach was evaluated in healthy volunteers and subjects with idiopathic pulmonary fibrosis (IPF).

Methods—A calibration scan determined the TE at which ^{129}Xe in RBCs and barrier were 90° out of phase. At this TE, interleaved dissolved and gas-phase images were acquired using a 3D radial acquisition and were reconstructed separately using the NUFFT algorithm. The dissolved-phase image was phase-shifted to cast RBC and barrier signal into the real and imaginary channels such that the image-derived RBC:barrier ratio matched that from spectroscopy. The RBC and barrier images were further corrected for regional field inhomogeneity using a phase map created from the gas-phase ^{129}Xe image.

Results—Healthy volunteers exhibited largely uniform ^{129}Xe-barrier and ^{129}Xe-RBC images. By contrast, ^{129}Xe-RBC images in IPF subjects exhibited significant signal voids. These voids correlated qualitatively with regions of fibrosis visible on CT.

Conclusions—This study illustrates the feasibility of acquiring single-breath, 3D isotropic images of ^{129}Xe in the airspaces, barrier, and RBCs using a 1-point Dixon 3D radial acquisition.

Corresponding Author: **Bastiaan Driehuys**, Center for In Vivo Microscopy, Box 3302, Duke University Medical Center, Durham, NC 27710, Phone (919) 684-7786, Fax (919) 684-7158, bastiaan.driehuys@duke.edu.

Keywords

1-point Dixon; Hyperpolarized xenon; 3D Radial

Introduction

While hyperpolarized (HP) ^{3}He MRI has enabled imaging of pulmonary structure, recent years have seen increasing progress demonstrating that HP ^{129}Xe can serve as a sustainable and economically viable replacement for this scarce gas (1). Like ^{3}He, ^{129}Xe provides a non-invasive, ionizing radiation-free probe of pulmonary structure (2) and airway patency. Additionally, HP ^{129}Xe is well-tolerated (3,4), enables quantitative ventilation imaging (2,5), and produces diffusion-weighted images that reveal emphysematous structural changes (6,7). However, the most significant opportunity is to use the solubility and chemical-shift of ^{129}Xe in the lung to visualize gas-exchange.

Upon inhalation, the bulk of the ^{129}Xe gas remains in the airspaces, but because it is soluble in pulmonary tissues (Ostwald solubility of 0.27 in red blood cells (RBCs) and 0.10 in barrier/blood-plasma (8)), a small fraction of ^{129}Xe enters these compartments. This dissolved-phase, in humans, is comprised of two distinct resonances corresponding to ^{129}Xe in interstitial tissue and plasma, referred to collectively as the barrier (198 ppm), and ^{129}Xe in the RBCs (217 ppm). Because ^{129}Xe traverses the same path as oxygen through the barrier to the RBCs, and because these compartments can be distinguished by their chemical-shift, ^{129}Xe has the potential to serve as an almost ideal probe of diffusive gas-exchange.

However, imaging the dissolved-phase ^{129}Xe is challenging given its short T_2^* of ~2 ms at 1.5T (9), and because the magnetization in these compartments is only 1–2 % of ^{129}Xe in the gas-phase (10). As a result, the early imaging efforts employed chemical-shift imaging (11), or indirect techniques such xenon polarization transfer contrast (12). However, the small dissolved-phase magnetization can be directly imaged as its magnetization is continuously replenished by ^{129}Xe diffusing in from the airspaces. Moreover, the short T_2^* can be overcome by employing 3D radial acquisitions that sample the FID with a sub-millisecond echo-time (TE). Recently, these insights have enabled direct 3D dissolved-phase imaging in human subjects within a single breath-hold (13). This technique was subsequently extended to concurrently acquire the gas-phase source distribution in the same breath (14), which led to the ability to quantify the impact of posture on the dissolved-phase distribution (15). However, these early approaches treated the dissolved-phase as a single entity, rather than individually quantifying ^{129}Xe in the barrier and RBC compartments.

The importance of separating ^{129}Xe gas-transfer into its barrier and RBC constituents was recently illustrated by spectroscopic studies of patients with idiopathic pulmonary fibrosis (IPF). IPF is a form of interstitial lung disease that is characterized by progressively increasing collagen deposition and interstitial inflammation (16). The associated thickening of the blood-gas barrier that impairs diffusive oxygen uptake also impairs the diffusive replenishment of ^{129}Xe magnetization in the RBCs. Consequently, global gas-transfer spectra demonstrated that the ratio of ^{129}Xe uptake in the RBCs vs. barrier (RBC:barrier)

was 3.3-fold lower in IPF patients than in healthy volunteers (10). Interestingly, this ratio correlated well with conventional physiologic measurements of gas-exchange (DL_{CO}, r=0.89). In healthy subjects, the RBC:barrier was sensitive to changes in capillary blood volume and alveolar pressure. Beyond these ratios, the frequency of ^{129}Xe in the RBC compartment appeared to be sensitive to oxygenation at the capillary level. Hence, this spectroscopic study suggests that if the RBC and barrier compartments could be individually visualized by imaging, such images could provide fundamental insights about regional gas-exchange.

Separating ^{129}Xe uptake in the barrier and RBCs is similar to the more familiar problem of fat-water separation in ^{1}H MRI (17). Like fat and water, which at 1.5T are separated by ~220 Hz, ^{129}Xe in the barrier and RBC compartments are separated by ~340 Hz. However, unlike ^{1}H in fat and water, ^{129}Xe in the pulmonary RBC and barrier tissues experience a very short T_2^*, which constrains the available acquisition time for typical, well-known Dixon techniques. Therefore, early efforts to generate separate images of ^{129}Xe in the barrier and RBCs in a rat model of fibrosis utilized the simpler 1-point Dixon technique (18). This approach acquires images at a single TE such that when the center of k-space is sampled, the two resonances are 90° out of phase. By subsequently phase-shifting the image, the RBC and barrier signals are largely confined to the real and imaginary receiver channels. This first study generated only 2D images, but the approach was recently extended to acquire 3D isotropic images of the two compartments in a rat model of late-stage fibrosis (19). Both studies showed that while the ^{129}Xe uptake in the barrier compartment was largely unaffected, ^{129}Xe uptake in RBCs was markedly reduced in fibrotic regions.

A significant advance in translating ^{129}Xe gas-transfer clinically was recently made by Qing *et al*. who separated the barrier and RBC images using the hierarchical IDEAL algorithm (20). This extension of the original IDEAL approach allows data to be acquired at multiple (and arbitrary) TEs, while the B_0 inhomogeneity is iteratively calculated and corrected at multiple resolution levels to decompose the RBC and barrier images. One challenge of the IDEAL algorithm is that it requires images to be acquired at 3 TEs, which is challenging given the short dissolved-phase T_2*. However, Qing *et al*. overcame this by employing very high ^{129}Xe polarizations and demonstrated well-separated images that correlated with global spectroscopic measures (20).

In this work, we present the clinical translation of the 1-point Dixon approach to separately image ^{129}Xe in the barrier and the RBCs using only a single, sub-millisecond TE. Such short TEs reduce T_2^* blurring and enable increased k-space sampling within a single breath-hold. By further acquiring an interleaved gas-phase image, we can image all three compartments in a single breath-hold. This single-resonance gas-phase image can be used to create a phase map and correct for B_0 inhomogeneity. As an initial test of this method, we chose to compare images acquired in healthy volunteers and patients with IPF. This patient population is advantageous as they experience significant diffusion-limitation caused by interstitial thickening of the blood-gas barrier, which reduces ^{129}Xe uptake in RBCs (10). Hence, ^{129}Xe gas-transfer to RBCs was expected to exhibit focal gas-transfer defects. Moreover, patients with IPF exhibit features of traction bronchiectasis, honeycombing,

reticular and ground glass opacities, and consolidation in their CT images, which helps to qualitatively validate the 1-point Dixon imaging approach.

Methods

Subject Inclusion and Exclusion Criteria

Studies were approved by the Duke Institutional Review Board and were conducted under IND 109,490. Written, informed consent was obtained from all subjects prior to the scan. Data was acquired in 4 healthy volunteers, and 3 subjects with IPF, one of whom was imaged again 9 months later. All subjects were at least 18 years of age (healthy volunteers – 3 men, 1 woman, age = 44.0 ± 19.4 years; IPF subjects – 3 men, age = 64.7 ± 8.7 years). The healthy volunteers had less than a 5 pack-year smoking history, had not smoked in the last 5 years, and had no diagnosed pulmonary disorders. Subjects were excluded if they had a history of cardiac arrhythmias, were pregnant or lactating, or had a respiratory illness within 30 days of MRI.

^{129}Xe Polarization and Delivery

Isotopically enriched ^{129}Xe (85%) was polarized to 10–15% by rubidium-vapor spin-exchange optical pumping (21) using a commercially available polarizer (Model 9800, Polarean, Inc., Durham, NC). Xenon was cryogenically accumulated and thawed into a Tedlar bag and polarization was determined using a polarization measurement station (Model 2881, Polarean, Inc.). Prior to gas inhalation, the subjects were instructed to inhale to total lung capacity and exhale to functional residual capacity twice. Subsequently, the contents of the bag were inhaled via a mouthpiece connected to the bag through a 6-mm ID Tygon tube, and the subjects held their breath for the duration of the scans (13–15 s). As explained below, to establish the correct TE for Dixon imaging, subjects first underwent a calibration scan, where they received a mixture of 400 ml of HP ^{129}Xe and 600 ml of ultra-high-purity N_2. For the subsequent gas-transfer image, subjects received a 1-L dose of HP ^{129}Xe. The subject's heart rate and oxygen saturation were monitored using an MR-compatible monitoring system (GE Healthcare, Helsinki Finland).

Image Acquisition and Reconstruction

The 1-point Dixon acquisition requires solving three problems. *First*, it is necessary to find the echo-time, $TE_{90,}$ at which the RBC and barrier resonances are 90° out of phase. *Second*, the image must be phase-shifted such that the RBC-dominant signal becomes aligned with the in-phase channel of the scanner, and the barrier-dominated image is aligned with the quadrature channel. And finally, the images must be further corrected for any phase variation caused by B_0 inhomogeneity. These steps are achieved as follows.

a) Calibration spectra to determine TE_{90}—In principle, the TE_{90} can be simply calculated based on the known RBC-barrier frequency difference (Δf), given by $TE_{90}=\frac{1}{4\Delta f}$. Hence, after application of a hypothetical infinitely short pulse, a frequency difference of 340 Hz would cause a 90° phase-difference to occur at TE_{90} = 735 μs. However, the RF pulse used to excite the dissolved-phase ^{129}Xe selectively is relatively long

(1.2 ms), and therefore significant phase evolution occurs before the magnetization reaches the transverse plane. Moreover, it has been shown that the TE_{90} varies according to the extent of fibrosis and inflammation because this changes ^{129}Xe compartmental exchange between the barrier and RBCs (19). Hence, for each subject in our study the TE_{90} was empirically determined as outlined in **Figure 1A**. In a single breath, dissolved-phase spectra were acquired in an interleaved manner, at four progressively longer TEs of 275, 375, 475, and 575 μs. (Echo time has been defined from the end of the 1.2-ms 3-lobe sinc pulse to acquisition of the first data point.) The other acquisition parameters were: number of points = 512, dwell-time = 16 μs, flip-angle = 22°, TR = 50 ms, NEX = 50. After acquisition of each spectrum, crusher gradients (amplitude = 3.3 G/cm, total duration = 3 ms) were played out on all three gradient axes to de-phase the long-lived off-resonance gas-phase signal. Once dissolved-phase spectra had been acquired, transmit and receive frequencies were changed to the gas-phase resonance (−3832 Hz) and a single gas-phase reference spectrum was acquired at TE = 275 μs.

The data were processed using routines written in MATLAB (The MathWorks, Inc., Natick, MA). The first 25 FIDs at each TE were discarded to avoid the presence of “downstream magnetization” from ^{129}Xe in the larger vasculature. The remaining 25 FIDs were averaged, exponentially line-broadened by 50 Hz, and Fourier transformed to generate a dissolved-phase spectrum with a small gas-phase reference peak. The complex spectrum was then fit using a non-linear least-squares optimization algorithm to a sum of Lorentzian and Dispersive functions to extract the amplitude, frequency, width, and phase of each resonance at each TE (10). The phase-difference between RBC and barrier was fit as a function of TE by linear-regression to determine the TE_{90}. Additionally, the spectrum acquired at a TE of 275 μs was used to calculate the area under the curve of each resonance, which was then used to calculate the ratio of the RBC and the barrier signals (RBC:barrier). As described later, this ratio was used in calculations that determined the receiver phase-offset required to align the RBC and barrier components of the dissolved-phase image to the real and imaginary receiver channels.

b) Image acquisition and workflow—Images were acquired on a 1.5-T scanner (GE EXCITE 15M4). Subjects were fitted with a quadrature vest coil tuned to the ^{129}Xe resonance frequency at 17.66 MHz (Clinical MR Solutions, Brookfield, WI). The coil was proton-blocked to enable ^{1}H imaging with the scanner’s body coil.

Single-breath gas and dissolved-phase images were acquired during a 15-sec breath-hold using 1-L of HP ^{129}Xe and a 3D radial sequence (15), with the TE set to the TE_{90}. Transmit and receive frequencies were alternated between the gas and RBC resonance (+3832 Hz) to acquire each radial ray of k-space, which were distributed pseudo-uniformly in both k-space and time using a 3D golden-means sampling strategy (20,22). [Acquisition parameters: 1200-μs sinc pulse, matrix=32×32×32, flip-angles = 0.5/22°, number of rays = 2002 (1001 at each frequency), FOV = 40 cm, TE/TR = TE_{90}/7.5 ms, receiver bandwidth = 15.625 kHz]. The gas and dissolved-phase data were separately reconstructed onto a 64×64×64 matrix using a NUFFT reconstruction algorithm (23) to generate isotropic, 3D gas and dissolved-phase images.

To help delineate the thoracic cavity, a 3D radial ^{1}H image was acquired during a separate 15-s breath-hold. In order to achieve approximately the same lung inflation as during the ^{129}Xe scan, the subject inhaled 1L of air from a polyethylene bag. These images were acquired using: 274-μs hard RF pulse, TE/TR = 0.199/2.4 ms, matrix = 64×64×64, number of rays = 5647, 512 dummy pulses to achieve steady state magnetization, flip-angle = 5°, bandwidth = 15.625 kHz, and FOV = 40 cm.

Image Processing and Analysis

a) Image registration and segmentation—In order to confine the analysis to the thoracic cavity, the ^{1}H images were registered to the ^{129}Xe gas-phase images via a multi-resolution affine transformation using the Image Registration Toolkit (24). The registered ^{1}H images were segmented using seed-based region growing implemented in 3DSlicer (2) to generate the thoracic cavity mask. This mask was morphologically closed using a spherical structuring element with a 7-voxel diameter, and 'filled' to remove any additional holes in the mask, and was then manually segmented to remove the major airways in MATLAB.

b) Determining the receiver phase offset—Although imaging at TE_{90} ensures that RBC and barrier signals are 90° out of phase relative to one another, the two compartments are not necessarily aligned with the real and imaginary receiver channels because the scanner imparts an arbitrary phase shift ϕ_0 to the data. Assuming the images were acquired at exactly TE_{90}, the signal (S) at the center of k-space (k_0) can be written as

$$S_{K_0} = (S_{RBC} + iS_{Barrier})\, e^{i\phi_0} \quad [1]$$

where S_{RBC} and $S_{Barrier}$ are the signal contributions from the RBC and barrier resonances. Applying a phase shift $\Delta\phi$, that is exactly opposite to ϕ_0 would align the RBC and barrier signals with the real and imaginary receiver channels, but it is not known a priori. Instead, applying an arbitrary phase shift $\Delta\phi$ yields a signal

$$S_{k_0}(\Delta\phi) = (S_{RBC} + iS_{Barrier})\, e^{i(\phi_0 + \Delta\phi)} \quad [2]$$

We now use the additional constraint that when the correct phase shift $\Delta\phi$ is applied, the ratio of the total RBC and barrier signal intensity within the thoracic cavity obtained from imaging, must match that measured by spectroscopy (10). We designate this spectroscopic ratio as R, and solve for $\Delta\phi$ using $S_{Re}(\Delta\phi)/S_{im}(\Delta\phi) = R$. To compute the real to imaginary ratio from the phase-shifted image, we expand the complex signal in Equation 2 into its real (S_{Re}) and imaginary (S_{Im}) components. By defining $S_{RBC} = R \times S_{barrier}$, the resulting ratio of the real and imaginary image data within the thoracic cavity can then be written as a function only of the phase shift $\Delta\phi$ applied, and the ratio R.

$$\frac{S_{Re}(\Delta\phi)}{S_{Im}(\Delta\phi)} = \frac{R\cos(\phi_0 + \Delta\phi) - \sin(\phi_0 + \Delta\phi)}{R\sin(\phi_0 + \Delta\phi) + \cos(\phi_0 + \Delta\phi)} \quad [3]$$

Note that when the correct phase shift $\Delta\phi = -\phi_0$ has been applied, equation 3 reduces to $S_{Re}/S_{Im} = R$, as required. Prior to making this calculation an additional correction must be made to account for the spectroscopic ratio having been acquired at a longer TR (50ms) compared to the imaging scan (effective TR of 15ms). The effect of TR on RBC:barrier ratio was estimated by solving the Ernst equation for steady-state RBC and barrier signals, but employing diffusive replenishment instead of the conventional thermal recovery term $1 - e^{-TR/T1}$. This calculation suggested the spectroscopic RBC:barrier ratio will be ~6.5% higher than the imaging ratio. Hence, the spectroscopic ratio R used to solve equation 3 was reduced by 6.5% prior to calculating the required receiver phase-offset. The phase shift $\Delta\phi$ was determined (**Figure 2A**) by plotting S_{Re}/S_{Im} over a range of receiver phase offsets [0, π] and fitting it to Equation 3 using a non-linear least-squares optimization algorithm. The dissolved image was then phase-shifted by $\Delta\phi = -\phi_0$ to align the RBC image to the real channel, and the barrier to the imaginary channel of the receiver.

c) Correcting for local phase inhomogeneity—The acquisition described thus far assumes that the only source of phase evolution between RBC and barrier is their frequency difference. However, phase differences can also be locally imparted by B_0 inhomogeneity. Fortunately, the inherently co-registered gas-phase ^{129}Xe image is comprised of only a single resonance, which makes any phase variation it exhibits attributable to B_0 inhomogeneity. Because gas-phase images were acquired at only a single TE, a phase-map was first generated, and then its mean was subtracted to create a 'differential phase map'. This differential phase map was then applied on a pixel-by-pixel basis to the RBC and barrier images to correct for B_0 inhomogeneity.

d) Maps of lung function—In addition to the native ^{129}Xe-barrier and ^{129}Xe-RBC images, several additional maps were found to be helpful in visualizing regional function. First, analogous to the spectroscopic RBC:barrier ratio, the RBC image was divided by the barrier image on a voxel-by-voxel basis to create an RBC:barrier map. Similarly, to gauge subtle differences in the RBC and barrier intensity, the RBC and barrier images were divided by the gas-phase images to yield the barrier:gas and RBC:gas maps (20). They were scaled by the 99th percentile of their cumulative distribution function (25) to limit their range to between 0 and 1.

Similar to ventilation images, the ^{129}Xe-RBC gas-transfer images were expected to exhibit regional gas-transfer defects in areas of fibrosis, and therefore gas-transfer defect maps were generated. The ^{129}Xe-RBC images were also scaled to range from 0 – 1, and only regions with a signal intensity lower than 0.1 were included in the gas-transfer defect map (25). The volume of gas-transfer defects was divided by the thoracic cavity volume to calculate the gas-transfer defect percentage. To test the validity of this imaging approach, a trained thoracic radiologist compared gas-transfer defects perceived in the ^{129}Xe-RBC images to structural features in the patient's CT images. The CT images were classified into three clusters of fibrotic severity – none, mild, severe, and the number of defects seen in each cluster were quantified.

Results

Single-breath images of ^{129}Xe in the gas and dissolved-phases were successfully acquired in all the subjects scanned and all dissolved-phase images were decomposed into the ^{129}Xe-barrier and ^{129}Xe-RBC images. Subject demographics are summarized in **Table 1**, along with spectroscopic and imaging-derived RBC:barrier ratios, RBC-barrier frequency differences, and the TE_{90}. This table also shows the data obtained in subject 3, 9 months after the initial scan (subject 3A).

As seen by the variability in TE_{90} and lack of correlation to RBC-barrier frequency difference, the phase calibration scan was important to accurately calculate the TE_{90} for each subject. Interestingly, although the RBC-barrier frequency difference was 40 Hz smaller in the IPF group, the resulting TE_{90} was actually shorter (0.24 ± 0.06 ms for IPF, 0.43 ± 0.03 ms for healthy). As shown in **Figure 1B**, increasing TE caused the phase difference between the RBC and barrier resonances to increase commensurately, as expected. For healthy volunteers, the relative phase accumulation with TE (slope) agreed with theoretical predictions (132.6 ± 4.7° ms^{-1} vs 119.8 ± 4.2° ms^{-1} predicted). The IPF patients, despite exhibiting a smaller RBC-barrier frequency difference, exhibited phase accumulation that was faster than expected (155.5 ± 18.2° ms^{-1} vs 110.7 ± 1.5° ms^{-1} predicted). Additionally, the linear-regression of RBC-barrier phase-difference as a function of TE yielded a positive intercept for all subjects; the intercept was moderately lower in the healthy volunteers (33.34 ± 4.1°) than in the IPF subjects (54.9 ± 9.5°).

The calculation of phase-shifts and their effects on the real and imaginary images are shown in **Figure 2**. The effect of phase-shift on image-derived RBC:barrier ratio is illustrated in **Figure 2A**. For this healthy subject with a corrected spectroscopic RBC:barrier ratio of R=0.43, a phase shift of $\Delta\varphi$ = 87.7° (inset) was needed to obtain the same ratio from imaging. After applying only the −87.7° phase shift, the real channel exhibits an apparent ‘defect’ in the basal portion of the left lung (white arrow, **Figure 2B**). However, this apparent defect originates from B_0 inhomogeneity, which is seen in the spatially varying phase of the single-resonance gas-phase image (**Figure 2C**). This map exhibited a phase ranging from about −45° to 45° across the lung, with the highest phase accumulation observed in the basal lung near the diaphragm. After correcting for this B_0 inhomogeneity, the apparent defect at the base of the lung has resolved (**Figure 2D**). Despite the visually apparent change in real and imaginary signal distribution seen in **Figure 2**, phase-correction only increased the image-derived RBC:barrier ratio minimally in this subject (0.43 to 0.44). In all healthy subjects, phase-map correction caused the RBC:barrier ratio to decrease by only −0.81 ± 1.48%. For the IPF subjects, it caused the RBC:barrier ratio to increase slightly (5.67 ± 1.79%.)

Figure 3 shows fully phase-corrected Dixon images depicting the ^{129}Xe-barrier and ^{129}Xe-RBC uptake along with the gas-phase ^{129}Xe distribution in a healthy volunteer and a subject with IPF. For the healthy volunteer, all three images are largely homogeneous with the signal intensity increasing moderately in the dependent lung. For the IPF subject, while the ventilation and barrier images are similarly homogenous, the RBC image-intensity is generally lower, and the images show widespread signal voids, or gas-transfer defects.

Interestingly, these gas-transfer defects in the RBC channel were present even in regions with seemingly normal gas-phase and barrier signal. Although gas-transfer defects were more prominent in the IPF subject, the healthy volunteer also exhibits some defects in the RBC map, most of which are located in well ventilated regions. The gas-transfer defect percentage was 11.51 ± 1.3% in the healthy volunteers, with defects predominantly located in the anterior, non-dependent portion of the lung. By contrast for the IPF subjects, the gas-transfer defect percentage was ~2-fold higher (22.4 ± 5.4%), and these defects were distributed in the peripheral and basal lung.

The ^{129}Xe-RBC images and their associated defect maps (yellow) were compared to the representative CT images available in the IPF subjects (**Figure 4**). Qualitatively, regions of fibrosis and opacification visible on CT, while generally remaining ventilated, exhibit prominent ^{129}Xe-RBC gas-transfer defects. In these IPF subjects, gas-transfer defects in both the posterior and anterior lung corresponded well to fibrosis seen on CT. Regions exhibiting fibrotic changes on CT contained ^{129}Xe-RBC defects 72% of the time. Because ^{129}Xe-RBC transfer is strongest in the posterior lung, these defects are most striking. Gas-transfer defects in the anterior lung, although also corresponding well to CT, could also be caused by lower SNR. Interestingly, 28% of the ^{129}Xe-RBC defects were in regions where the CT scan appeared normal.

Additional insights can be gained by examining the various ratio maps—barrier:gas, RBC:gas, and RBC:barrier shown in **Figure 5**. In the healthy volunteer, both the barrier:gas and RBC:gas maps appear relatively homogeneous, whereas the RBC:barrier map seems to exhibit increased ratios in the mid-lung gravitational plane. In the IPF subject, only the barrier:gas map remains moderately homogeneous. However, the RBC:gas map exhibits reduced overall intensity compared to the healthy volunteer, as well as numerous gas-transfer defects. The RBC:barrier map is also quite striking in the IPF subject, and while showing lower values overall, this map shows a few focal regions of high gas-transfer, with significantly lowered RBC:barrier at the peripheral and basal lung regions.

Discussion

Although demonstrated here in only a small patient population, this work provides preliminary evidence that the 1-point Dixon technique can produce isotropic 3D images of ^{129}Xe distribution in the airspaces and its transfer to the barrier and RBC compartments in a single-breath. This approach, while currently requiring an additional calibration scan, offers a simple alternative to the IDEAL algorithm to create separate images of ^{129}Xe uptake in the RBC and barrier compartments, through its utilization of only a single echo-time. A direct comparison of these two approaches in the same patient population should illuminate the relative benefits of each for enabling routine clinical gas-exchange MRI.

The 1-point Dixon approach requires accurately calibrating the TE required for a 90° RBC-barrier phase separation. It was interesting to note the variability of this TE_{90} relative to the calculated value and across groups. Such variability has been observed in prior studies of Dixon imaging including transgenic mice expressing human hemoglobin (26) and bleomycin-instilled rats (19). For healthy volunteers, TE_{90} was almost 300μs shorter (429μs)

than the theoretical predictions. Moreover, for IPF subjects, the calibrated TE_{90} was 194μs shorter than for healthy volunteers, even the RBC-barrier frequency difference in this population was 40Hz lower. For all subjects, the RBC-barrier phase evolution varied linearly with TE, and the fit exhibited a positive intercept (33.3°, healthy volunteers; 53.9° in IPF subjects), which suggests that significant phase evolution occurred during the RF pulse. These observations, along with lower TE_{90} in the IPF subjects may be in part explained by the different nature of susceptibility gradients and the variability in compartmental exchange in lungs affected by interstitial thickening and fibrosis. Ultimately, as discussed by Cleveland *et al*., these observations must be investigated by simulating the Bloch equations to better understand phase accumulation occurring during the RF pulse (19).

The 1-point Dixon acquisition has typically required additional reference scans to determine the receiver phase offset (phase error) and correct for the effects of field inhomogeneity (17). While, in principle, the receiver phase-offset could be determined using the phases of the calibration spectra, we have found that significant receiver phase-shifts can occur over time. On our scanner, we have seen receiver phase drift by as much as 100° in 10 minutes. Hence, we developed an approach that was immune to such drift by constraining the RBC:barrier ratio derived from imaging to match the spectroscopic ratio. This is somewhat similar to the ‘virtual shimming’ method introduced for the single-point Dixon based fat-water separation (27). In addition to determining the receiver phase offset, most multi-point Dixon methods (IDEAL, hierarchical IDEAL) correct for regional phase inhomogeneity by iteratively solving for a phase map (20,28). Here, ^{129}Xe Dixon MRI is advantageous because the single-resonance gas-phase image acquired in the same breath provides a map of regional inhomogeneity. Moreover, an additional advantage of the relatively low ^{129}Xe gyromagnetic ratio combined with imaging at 1.5T and relatively short TE is that phase did not change by more than 90° across the lung and hence did not require phase unwrapping (17). Thus, other than requiring a calibration scan, the strategy proposed here uses the acquired data to correct the receiver phase-offset and the regional field-inhomogeneity and provides images of all three resonances of ^{129}Xe in a single breath. With further work, the calibration scan could be eliminated by simply tracking the phase evolution from a single oversampled calibration FID that is appended to the image acquisition.

As shown in **Figure 4**, separation of ^{129}Xe transfer to the RBCs depicted defects that qualitatively corresponded to regions of fibrosis seen on CT. Perhaps more interesting are gas-transfer defects that were detected in regions where the CT appeared normal. These defects could indicate subtle regional inflammation that causes diffusion-limitation. It is conceivable that such regions represent earlier-stage disease that could potentially respond to therapy. In regions of impaired RBC transfer, the barrier images frequently exhibited increased signal. This, observation is consistent with inflammation and increased tissue deposition expected in IPF. However, some RBC defects also exhibited lower barrier signal, which can occur if xenon solubility in local tissue is reduced. Xenon solubility may be enhanced in the presence of inflammation, but reduced in the presence of collagen deposition or scarring. It is this solubility dependence that makes the barrier image more

challenging to interpret, but could also provide opportunities to identify regionally active disease.

Although we hypothesize that defects in the ^{129}Xe-RBC image of IPF patients are primarily caused by thickening of the blood-gas barrier, we cannot distinguish this effect from regionally reduced perfusion and capillary blood volume. Such discrimination could be done by also acquiring a high-resolution Gd-enhanced perfusion image (29). Moreover, because ^{129}Xe transfer into barrier and RBCs follows Fick's first law, it also depends on the alveolar surface-volume ratio. Thus, loss of alveolar surface area would cause both RBC and barrier intensity to diminish. Hence, RBC:barrier maps provide a potentially useful means to distinguish the two conditions.

Although the 1-point Dixon acquisition offers a simple method to independently image the dissolved ^{129}Xe resonances, it does have challenges. *First*, this method requires two well-separated resonances. However, both dissolved-phase resonances are broad (~140 Hz), and in healthy volunteers, overlap by 30 – 40%, which cannot be perfectly separated. An alternative strategy may be to employ chemical shift imaging. Although it sacrifices speed and resolution, it generates complete spectra for each voxel and could thus serve as a gold standard (11). *Second*, the Dixon condition is truly satisfied only at the center of k-space (k_0), beyond which, the ^{129}Xe-barrier resonance will continue to lag further in phase. This continued phase accumulation may be corrected using the modified IDEAL algorithm (28).

Conclusions

The 1-point Dixon strategy was successfully used to create isotropic 3D images of ^{129}Xe in the airspaces, barrier, and the RBCs within a single breath-hold. The method we propose is relatively simple to implement and depicts focal gas-transfer defects in IPF patients. While the current hypothesis assumes that the primary reason for reduced ^{129}Xe-RBC signal is diffusion-limitation, future experiments will include a Gd-perfusion scan to quantify potential changes in regional capillary blood volume. Additionally, understanding the root cause of the phase evolution may negate the need to calibrate the TE_{90}, leading to a single scan exam. Additionally, because the Dixon condition is satisfied only at the center of k-space, future studies will employ an iterative means to estimate the barrier and RBC images to correct for the continued phase accumulation during data acquisition (28). Given the good correlation between the ^{129}Xe-RBC and CT images, these preliminary results show that the ^{129}Xe-RBC images offer an ionizing-radiation-free, non-invasive means to visualize diffusive gas-exchange in the lung. With both the IDEAL technique and the present method established on a sound technical footing, the way is open for larger-scale clinical studies of ^{129}Xe gas-exchange MRI in interstitial lung disease.

Acknowledgements

The authors would like to thank Mr. John Davies for subject monitoring, Dr. Zackary I. Cleveland for helpful discussions, and Sally Zimney for carefully proofreading this manuscript. This work was funded by NIH/NHLBI R01 HL105643 and partly by the Center for In Vivo Microscopy NIBIB P41 EB015897, Duke CTSA Grant UL1 RR024128 from NCRR/NIH, and AI 081672.

References

1. Shea, DA.; Morgan. The Helium-3 Shortage: Supply, Demand, and Options for Congress; CRS Report for Congress 2010;
2. Virgincar RS, Cleveland ZI, Kaushik SS, Freeman MS, Nouls J, Cofer G, Martinez-Jimenez S, He M, Kraft M, Wolber J, McAdams HP, Driehuys B. Quantitative Analysis Of Hyperpolarized ^{129}Xe Ventilation Imaging In Healthy Volunteers And Subjects With Chronic Obstructive Pulmonary Disease. NMR Biomed. 2012; 26:424–435. [PubMed: 23065808]
3. Driehuys B, Martinez-Jimenez S, Cleveland ZI, Metz GM, Beaver DM, Nouls JC, Kaushik SS, Firszt R, Willis C, Kelly KT, Wolber J, Kraft M, McAdams HP. Chronic Obstructive Pulmonary Disease: Safety and Tolerability of Hyperpolarized Xe-129 MR Imaging in Healthy Volunteers and Patients. Radiology. 2012; 262(1):279–289. [PubMed: 22056683]
4. Shukla Y, Wheatley A, Kirby M, Svenningsen S, Farag A, Santyr GE, Paterson NA, McCormack DG, Parraga G. Hyperpolarized ^{129}Xe Magnetic Resonance Imaging: Tolerability in Healthy Volunteers and Subjects with Pulmonary Disease. Academic Radiology. 2012; 19(8):941–951. [PubMed: 22591724]
5. Mugler JP, Altes TA. Hyperpolarized 129Xe MRI of the human lung. J Magn Reson Imaging. 2013; 37(2):313–331. [PubMed: 23355432]
6. Kaushik SS, Cleveland ZI, Cofer GP, Metz G, Beaver D, Nouls J, Kraft M, Auffermann W, Wolber J, McAdams HP, Driehuys B. Diffusion-Weighted Hyperpolarized Xe-129 MRI in Healthy Volunteers and Subjects With Chronic Obstructive Pulmonary Disease. Magn Reson Med. 2011; 65(4):1155–1165.
7. Kirby M, Svenningsen S, Owrangi A, Wheatley A, Farag A, Ouriadov A, Santyr GE, Etemad-Rezai R, Coxson HO, McCormack DG. Hyperpolarized 3He and 129Xe MR imaging in healthy volunteers and patients with chronic obstructive pulmonary disease. Radiology. 2012; 265(2):600–610. [PubMed: 22952383]
8. Chen RY, Fan FC, Kim S, Jan KM, Usami S, Chien S. Tissue-blood partition coefficient for xenon: temperature and hematocrit dependence. J Appl Physiol. 1980; 49(2):178–183. [PubMed: 7400000]
9. Mugler, JP.; Altes, TA.; Ruset, IC.; Miller, GW.; Mata, JF.; Qing, K.; Tsentalovich, I.; Hersman, FW.; Ruppert, K. Image-based measurement of T2* for dissolved-phase Xe129 in the human lung; Proceedings of the International Society for Magnetic Resonance in Medicine; Melbourne, Australia. 2012.
10. Kaushik SS, Freeman MS, Yoon SW, Liljeroth MG, Stiles JV, Roos JE, Foster WM, Rackley CR, McAdams HP, Driehuys B. Measuring Diffusion-Limitation with a Perfusion-Limited Gas-Hyperpolarized 129Xe Gas-Transfer Spectroscopy in Patients with Idiopathic Pulmonary Fibrosis. J Appl Physiol. 2014; 117:577–585. [PubMed: 25038105]
11. Swanson SD, Rosen MS, Coulter KP, Welsh RC, Chupp TE. Distribution and dynamics of laser-polarized Xe-129 magnetization in vivo. Magn Reson Med. 1999; 42(6):1137–1145. [PubMed: 10571936]
12. Ruppert K, Brookeman JR, Hagspiel KD, Mugler JP. Probing lung physiology with xenon polarization transfer contrast (XTC). Magn Reson Med. 2000; 44(3):349–357. [PubMed: 10975884]
13. Cleveland ZI, Cofer GP, Metz G, Beaver D, Nouls J, Kaushik SS, Kraft M, Wolber J, Kelly KT, McAdams HP, Driehuys B. Hyperpolarized Xe-129 MR imaging of alveolar gas uptake in humans. Plos One. 2010; 5(8)
14. Mugler JP, Altes TA, Ruset IC, Dregely IM, Mata JF, Miller GW, Ketel S, Ketel J, Hersman FW, Ruppert K. Simultaneous magnetic resonance imaging of ventilation distribution and gas uptake in the human lung using hyperpolarized xenon-129. Proc Natl Acad Sci U S A. 2010; 107(50): 21707–21712. [PubMed: 21098267]
15. Kaushik SS, Freeman MS, Cleveland ZI, Davies J, Stiles J, Virgincar RS, Robertson SH, He M, Kelly KT, Foster WM, McAdams HP, Driehuys B. Probing the regional distribution of pulmonary gas exchange through single-breath gas- and dissolved-phase 129Xe MR imaging. J Appl Physiol. 2013; 115(6):850–860. [PubMed: 23845983]

16. Raghu G, Collard HR, Egan JJ, Martinez FJ, Behr J, Brown KK, Colby TV, Cordier J-F, Flaherty KR, Lasky JA, Lynch DA, Ryu JH, Swigris JJ, Wells AU, Ancochea J, Bouros D, Carvalho C, Costabel U, Ebina M, Hansell DM, Johkoh T, Kim DS, King TE, Kondoh Y, Myers J, Müller NL, Nicholson AG, Richeldi L, Selman M, Dudden RF, Griss BS, Protzko SL, Schünemann HJ. An Official ATS/ERS/JRS/ALAT Statement: Idiopathic Pulmonary Fibrosis: Evidence-based Guidelines for Diagnosis and Management. American Journal of Respiratory and Critical Care Medicine. 2011; 183(6):788–824. [PubMed: 21471066]
17. Ma JF. Dixon techniques for water and fat imaging. J Magn Reson Imaging. 2008; 28(3):543–558. [PubMed: 18777528]
18. Driehuys B, Cofer GP, Pollaro J, Mackel JB, Hedlund LW, Johnson GA. Imaging alveolar-capillary gas transfer using hyperpolarized Xe-129 MRI. Proc Natl Acad Sci U S A. 2006; 103(48):18278–18283. [PubMed: 17101964]
19. Cleveland ZI, Virgincar RS, Qi Y, Robertson SH, Degan S, Driehuys B. 3D MRI of impaired hyperpolarized 129Xe uptake in a rat model of pulmonary fibrosis. NMR Biomed. 2014 doi: 10.1002/nbm.3127.
20. Qing K, Ruppert K, Jiang Y, Mata JF, Miller GW, Shim YM, Wang C, Ruset IC, Hersman FW, Altes TA, Mugler JP. Regional mapping of gas uptake by blood and tissue in the human lung using hyperpolarized xenon-129 MRI. J Magn Reson Imaging. 2014; 39(2):346–359. [PubMed: 23681559]
21. Driehuys B, Cates GD, Miron E, Sauer K, Walter DK, Happer W. High-volume production of laser-polarized Xe-129. Appl Phys Lett. 1996; 69(12):1668–1670.
22. Chan RW, Ramsay EA, Cunningham CH, Plewes DB. Temporal stability of adaptive 3D radial MRI using multidimensional golden means. Magn Reson Med. 2009; 61(2):354–363. [PubMed: 19165897]
23. Song JY, Liu YH, Gewalt SL, Cofer G, Johnson GA, Liu QH. Least-square NUFFT methods applied to 2-D and 3-D radially encoded MR image reconstruction. IEEE Trans Biomed Eng. 2009; 56(4):1134–1142. [PubMed: 19174334]
24. Studholme C, Hill DLG, Hawkes DJ. An overlap invariant entropy measure of 3D medical image alignment. Pattern Recognit. 1999; 32(1):71–86.
25. He M, Kaushik SS, Robertson SH, Freeman MS, Virgincar RS, McAdams HP, Driehuys B. Extending Semiautomatic Ventilation Defect Analysis for Hyperpolarized 129Xe Ventilation MRI. Academic Radiology. 2014; 21(12):1530–1541. [PubMed: 25262951]
26. Freeman MS, Cleveland ZI, Qi Y, Driehuys B. Enabling hyperpolarized 129Xe MR spectroscopy and imaging of pulmonary gas transfer to the red blood cells in transgenic mice expressing human hemoglobin. Magn Reson Med. 2013; 70(5):1192–1199. [PubMed: 24006177]
27. Xiang, Q-S. Improved Single Point Water-Fat Imaging with Virtual Shimming; Proceedings of the International Society of Magnetic Resonance in Medicine; Glasgow, Scotland. 2001.
28. Brodsky EK, Holmes JH, Yu HZ, Reeder SB. Generalized k-space decomposition with chemical shift correction for non-cartesian water-fat Imaging. Magn Reson Med. 2008; 59(5):1151–1164. [PubMed: 18429018]
29. Bauman G, Johnson KM, Bell LC, Velikina JV, Samsonov AA, Nagle SK, Fain SB. Three-dimensional pulmonary perfusion MRI with radial ultrashort echo time and spatial–temporal constrained reconstruction. Magn Reson Med. 2014 doi: 10.1002/mrm.25158.

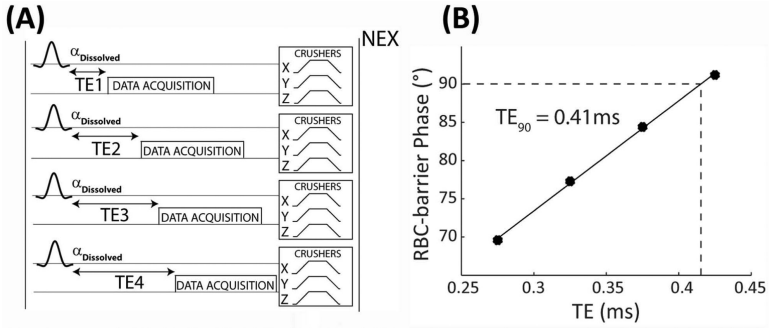

Figure 1.

The phase calibration scan shown in (A) acquires dissolved-phase spectra at 4 echo times (275, 375, 475, 575 μs) with a NEX of 50. Crusher gradients are played out on all three gradient axes to de-phase any off-resonant gas-phase signal. The last 25 dissolved-phase FIDs are averaged together and fit to a sum of Lorentzian and Dispersive functions to extract the phase difference between the RBC and barrier resonances. These phase differences are plotted as a function of echo time (B) and fit to a line to calculate the TE_{90}.

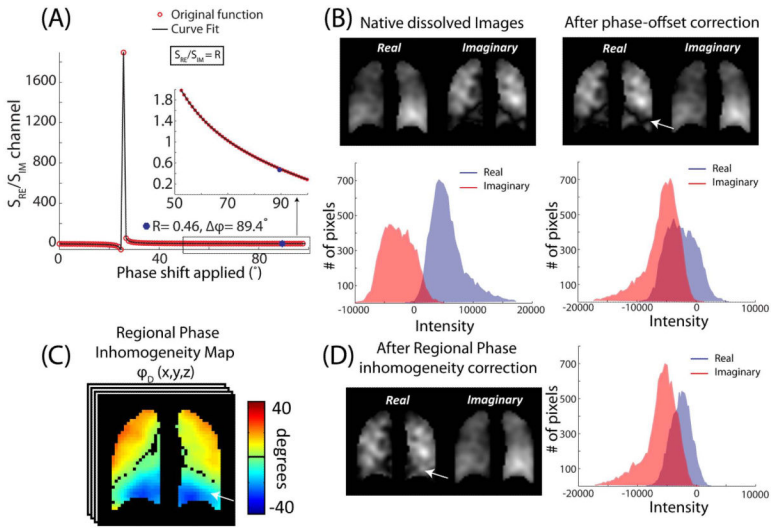

Figure 2.

Phase correcting the dissolved-phase images. (A) The ratio of the sum of the real and imaginary channels as a function of receiver phase applied. The inset shows the approach to the spectroscopic RBC:barrier ratio. For this subject, a receiver phase offset of −87.7° makes the ratio of real and imaginary channel signals equal to the spectroscopic ratio R=0.43. (B) Magnitude images of the real and imaginary channel after applying the calculated receiver phase offset. As shown by the white arrow, this subject exhibits a low intensity stripe at the base of the lung in the real channel. This may be partly caused by the abrupt change in the regional phase as shown by the difference phase map (C). Once the regional phase inhomogeneity correction was applied, this apparent defect was removed (D).

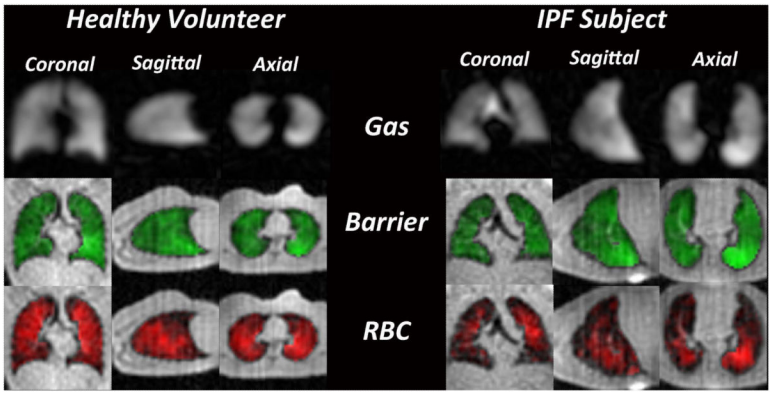

Figure 3.

Representative single breath images of ^{129}Xe in the gas-phase (grayscale), barrier tissues (green), and RBCs (red). In the healthy volunteer distribution of ^{129}Xe in all three resonances was largely homogeneous. In the IPF subject gas-phase and barrier images exhibit largely homogeneous intensity, but the RBC image contains widespread gas-transfer defects.

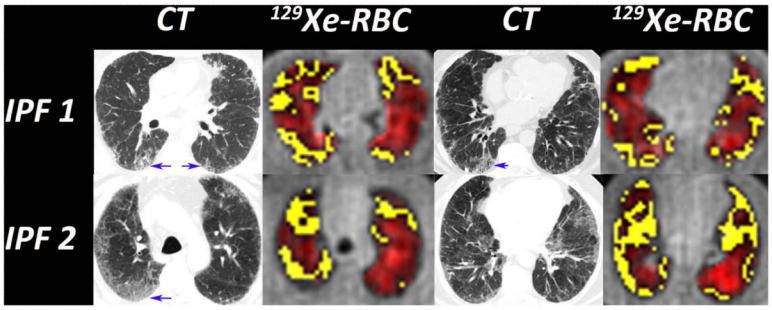

Figure 4.

The ^{129}Xe-RBC images show numerous gas-transfer defects (yellow) that qualitatively correlate with regions of fibrosis seen on CT (blue arrows). Gas-transfer defects were also found in regions that had no visible fibrosis on CT. These could point to regions of subtle inflammation or early fibrosis that may respond to therapy.

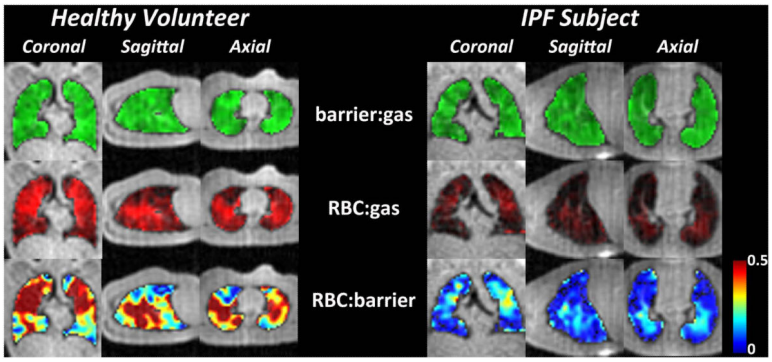

Figure 5.

Ratios of the ^{129}Xe-barrier:gas, ^{129}Xe-RBC:gas, and the RBC:barrier images. Unlike the ^{129}Xe-RBC images seen in figure 3, compared to the healthy volunteer, the signal intensity of the RBC:gas images are dramatically different in the IPF subject. Similarly, the RBC:barrier maps in the IPF subject show dramatically reduced ^{129}Xe uptake by the RBCs.

Table 1

Subject demographics, spectroscopic and imaging-derived parameters. The imaging derived RBC:barrier ratio is after regional phase inhomogeneity correction.

Subject #	Age (years)	RBC:barrier			Δf (Hz)	TE_{90} (μs)
		Spectroscopy	TR-corrected ratio	Imaging		
Healthy Volunteers						
1	56	0.49	0.46	0.45	349.9	411
2	65	0.53	0.50	0.50	328.9	407
3	29	0.46	0.43	0.44	323.0	470
4	26	0.64	0.60	0.59	330.1	427
IPF Subjects						
1	72	0.16	0.15	0.16	311.8	285
2	67	0.16	0.15	0.16	303.4	163
3	55	0.17	0.16	0.14	287.3	259
3A	55	0.14	0.13	0.13	307.5	256